PHYSICAL REVIEW B **83**, 165318 (2011)

Thermodynamic stability and growth kinetics of epitaxial $SrTiO_3$ on silicon

A. M. Kolpak and S. Ismail-Beigi
Center for Research on Interface Structures and Phenomena and Department of Applied Physics, Yale University, New Haven, Connecticut 06520-8284, USA

(Received 20 December 2010; revised manuscript received 14 March 2011; published 25 April 2011)

We determine the thermodynamic phase diagram of the epitaxial $SrTiO_3$/Si heterostructure from first-principles density functional theory calculations. We demonstrate that the system is not thermodynamically stable with respect to formation of an interfacial SiO_2 region under any experimentally attainable oxygen partial pressures. To understand the experimental observation of an atomically abrupt interface without a SiO_2 layer, we construct a kinetic model of the growth process. We show that the observed stability of the nonequilibrium interface under both growth and ambient conditions is directly related to the interface chemistry, which gives rise to a large (2.2 eV) barrier for oxygen diffusion to the interface layer and kinetically traps an atomically abrupt interface structure. Our model leads to the prediction of an interface structure in good agreement with experiment, demonstrating that a combination of first-principles computations, thermodynamics, and simple kinetic modeling can be used to determine non + -thermodynamic equilibrium atomic structures in complex heterosystems.

DOI: 10.1103/PhysRevB.83.165318 PACS number(s): 68.35.Fx, 81.15.Aa

I. INTRODUCTION

Experimental advances in growth procedures such as molecular beam epitaxy (MBE) and pulsed laser deposition (PLD) have made it possible to grow epitaxial, coherent oxide films with close to atomically abrupt interfaces on a number of substrates,[1] leading to an array of novel physics and potential applications. Even with knowledge of the atomic layer-by-layer deposition procedure, however, it is difficult to predict the atomic structure and composition of the as-grown heterostructures. While experimental structural characterization can provide a great deal of information, determining the position and identity of every atom in a macroscopic structure remains a daunting, and often impossible, task. Yet knowledge of the precise interface structure is extremely important for understanding the physical properties of the heterostructure, as demonstrated, for example, by the importance of the interface composition and structure for electronic band energy alignments in semiconductor/oxide devices.[2–4]

Theoretical studies using first-principles methods such as density functional theory (DFT) are essential for determining the atomic-level structural and electronic information of heterostructures, but they also have important limitations. One, of course, is the well-known band-gap underestimation in DFT.[5] Even more elementary, however, is the fact that DFT predicts the zero-temperature, electronic ground state for any atomic configuration. Determining the atomic configuration and elemental composition of the thermodynamic ground state is a separate problem, requiring some type of efficient sampling of the possible atomic arrangements. If one can narrow down this phase space by making reasonable assumptions about the structure, either from experimental data or physical or chemical intuition, performing a thermodynamic analysis enables the prediction of the thermodynamic ground state atomic structure as a function of environmental conditions.[6] For heterostructures grown with MBE and PLD, however, determining the atomic structure is even more challenging because the systems are often grown out of equilibrium, and sometimes can *only* be grown out of equilibrium, as exemplified below for the $SrTiO_3$/Si system. So how does one predict the resulting metastable, kinetically trapped structures?

One can attempt to simulate the kinetic process itself via molecular dynamics[7] or kinetic Monte Carlo methods.[8] However, using these techniques with first-principles electronic structure methods significantly limits the time scales that are accessible due to the intense computational costs of methods such as DFT when applied to complex heterostructures. Speedups usually involve the use of model potentials or choosing a limited set of pathways to be explored ahead of time (e.g., Ref. 8), assumptions which may be good and verifiable for bulk environments but which can have significant problems when applied to heterostructures where the interfacial chemistry and microscopic dynamics is ill understood.

In this paper, we use the epitaxial $SrTiO_3$/Si system as an example of a situation in which one can successfully apply a combination of DFT, experimental input, thermodynamic analysis, and simple kinetic modeling to predict a nonthermodynamic equilibrium structure. Due to the complexity of the materials system, none of these methods is alone sufficient; rather, we employ a judicious combination of all of them to narrow down the possibilities to the point at which we can use the power of first-principles theory to properly understand the system. In the process, we demonstrate that the interface-chemistry-based kinetic trapping mechanism in this system is the key step enabling the epitaxial growth of $SrTiO_3$/Si. This understanding may have important implications for the growth of other epitaxial oxides on semiconductors, which has been largely unsuccessful to date.[9]

The remainder of the paper is arranged as follows. In Sec. II, we describe the theory and methods behind the thermodynamic analysis. In Sec. III we present the interface phase diagram and discuss both its limitations and its utility in nonequilibrium structure determination. In Sec. IV, we develop a kinetic model of the $SrTiO_3$/Si growth procedure, describe the mechanism by which an atomically abrupt interface is kinetically trapped, and predict the experimentally realized interface structure, which we show is in good agreement with experimental data.

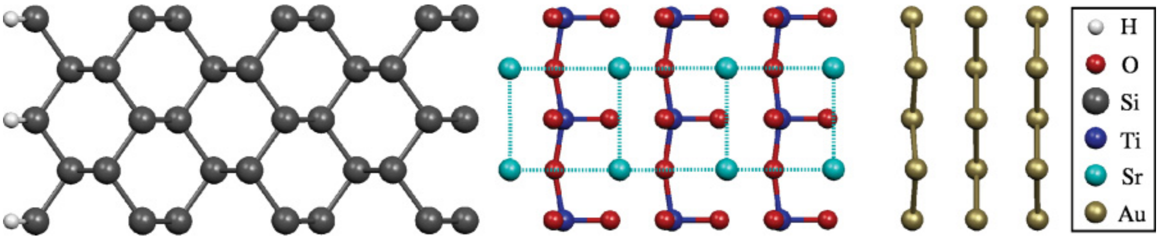

FIG. 1. (Color online) An example simulation supercell, showing the relaxed atomic structure of the experimentally realized interface composition.

Finally, we conclude with a discussion of the implications of the kinetic trapping mechanism for the epitaxial growth of other perovskite oxides on silicon.

II. THEORY AND METHODS

A. Computational details

DFT calculations are performed within the generalized gradient approximation (GGA) using the DACAPO and PWSCF codes[10,11] and ultrasoft pseudopotentials[12] with a 30 Ry cutoff energy. All supercells are composed of a 13-atomic layer-thick, H-passivated Si substrate, an interfacial layer, and 3–9 unit cells of $SrTiO_3$. The $SrTiO_3/Si$ heterostructures have a (001) interface. The $SrTiO_3$ film is terminated with a SrO plane, and capped by a gold electrode. An example of a simulation supercell is shown in Fig. 1. The electronic and structural properties of the slabs are well converged with respect to both the Si and electrode thickness in addition to the k-point sampling ($4 \times 8 \times 1$ Monkhorst-Pack) and Fermi temperature (0.05 eV). Periodic copies of the supercell are separated by $\approx$12 Å in the z direction (perpendicular to the interface), and a (2×1) supercell is used in the xy plane to allow for the formation of canonical Si dimers. Calculations are also performed for several structures with ($n \times 1$) symmetry, where $n = 3,4,5$. Tests using $c(2 \times 2)$ in-plane supercells for several interface compositions show no evidence of octahedral rotations in the $SrTiO_3$ film. The in-plane lattice constant is fixed to the theoretical Si lattice constant ($a = 3.866$ Å), resulting in a 1.7% compressive strain on the $SrTiO_3$, which is very close to the experimental strain at room temperature.[13] In all calculations presented in this work, all atoms are relaxed completely until forces on each are <0.01 eV/Å. Diffusion barriers are determined with the nudged elastic band (NEB) method[14] with no additional constraints imposed on the atoms.

B. Interface compositions

The interfacial layer, which is defined as the atomic plane adjacent to both a full atomic layer of silicon and a full atomic layer of either SrO or TiO_2 (see Fig. 1), is varied by changing the number of Sr, Ti, Si, and O atoms. The initial $SrTiO_3$ plane is also varied, so that the interface layer is in contact with either a SrO or a TiO_2 plane. In addition, for a given composition the relaxed structures and total energies of several possible registries between the film and the silicon substrate are computed; below, only the lowest-energy structure for each composition is considered. The interface compositions studied include but are not limited to the previously proposed structures,[2,4,15–20] for a total of 56 compositions. Representative atomic structures from our library are illustrated in the Appendix.

C. Thermodynamic extrapolation

One can use a thermodynamic analysis to determine the lowest-free-energy structure from a set of atomic structures with different compositions. If the set of structures forms a reasonable representation of the available phase space, one can then predict from DFT the total energy of the most favorable structure under given environmental conditions. Theoretically, these conditions are represented by a set of chemical potentials for each element. This corresponds to assuming that each element in the system is in equilibrium with a physical reservoir such as a gas, a surface phase, or a bulk phase. Using standard thermodynamic data for the various reservoirs, the chemical potentials can be correlated to temperature and partial pressure for comparison with experimental conditions. In the following, we describe this approach for the $SrTiO_3/Si$ heterosystem.

1. Computation of the Gibbs free energy

To determine the thermodynamic stability of the various interface compositions, we compute their Gibbs free energy to construct a phase diagram for the heterosystem. The Gibbs free energy of the heterostructure per interfacial unit cell is

$$\Delta G_{\rm int}(T,p_i) = \frac{1}{m}\left\{\Delta G^0_{\rm f,int}(T,p_i) - \sum_i n_i^{\rm int}\mu_i(T,p_i)\right\}, \qquad (1)$$

where m is the number of two-dimensional (2D) unit cells, $\Delta G^0_{\rm f,int}(T,p_i)$ is the interface formation free energy at temperature T with p_i being the partial pressure of species i, $n_i^{\rm int}$ is the number of atoms of species i in the interfacial region, and $\mu_i(T,p_i)$ is the chemical potential of species i, where i is O, Sr, Ti, or Si. We will assume that all of the temperature and pressure dependence of $\Delta G_{\rm int}$ is contained within the chemical potentials $\mu_i(T,p_i)$, which include, for example, the entropy of the gas phase molecules. In other words, $\Delta G^0_{\rm f,int}(T,p_i) \approx \Delta E_{\rm f,int}$, the total energy of interface formation at $T = 0$. This approximation discards the pressure dependence of the free energy of the heterostructure (which is negligible) but more importantly assumes that the entropic contribution of the heterostructure, primarily the vibrational entropy, is roughly equal to the sum of the entropic contributions from the bulk constituents and is thus canceled out in $\Delta G_{\rm int}$. The above expression for ΔG also lacks terms due to temperature-dependent polarization, but we believe this is not an important factor as experiments demonstrate constant polar distortions as a function of temperature in the $SrTiO_3$/Si system.[21]

The total energy of interface formation, which is obtained directly from DFT calculations, is defined as

$$\Delta E_{\mathrm{f,int}} = E_{\mathrm{tot}} - m E_{\mathrm{ref}} - \sum_i n_i^{\mathrm{int}} E_i^{\mathrm{s.s.}} - E_{\mathrm{nonstoich}}^{\mathrm{corr}}. \qquad (2)$$

Here E_{tot} is the computed total energy of the Si/interface/$SrTiO_3$/electrode supercell, $E_i^{\mathrm{s.s.}}$ is the total energy of an atom of species i in its standard state at $T = 300$ K and $p = 1$ atm (e.g., Sr and Ti metals, O_2 gas),[22] and the reference energy is

$$E_{\mathrm{ref}} = E_{\mathrm{silicon}}^{\mathrm{slab}} + n E_{\mathrm{SrTiO_3}}^{\mathrm{bulk}} + E_{\mathrm{elec}} \, ,$$

where $E_{\mathrm{silicon}}^{\mathrm{slab}}$ and E_{elec} are the total energies of the silicon slab and the electrode, respectively, and $E_{\mathrm{SrTiO_3}}^{\mathrm{bulk}}$ is the total energy of a segment of bulk strained $SrTiO_3$ of the same thickness as the $SrTiO_3$ slab in the calculation. The final term in Eq. (2) is

$$E_{\mathrm{nonstoich}}^{\mathrm{corr}} = E_{\mathrm{SrO}}^{\mathrm{bulk}} + \alpha \Delta E_{\mathrm{SrO}}^{\mathrm{bind}} \, ,$$

where $E_{\mathrm{SrO}}^{\mathrm{bulk}}$ is the total energy per formula unit of bulk SrO and $\Delta E_{\mathrm{SrO}}^{\mathrm{bind}}$ is the computed binding energy of an SrO layer to the TiO_2-terminated surface of a stoichiometric $SrTiO_3$ (001) slab. This term allows for direct comparison between stoichiometric and nonstoichiometric $SrTiO_3$ films so that structures with either SrO ($\alpha = 1$) or TiO_2 ($\alpha = 0$) layers adjacent to the interface region have the same SrO/electrode termination.

2. *Constraints on the chemical potentials*

Both the temperature T and the oxygen partial pressure p_{O_2} are directly controlled during each step of the experimental growth procedure. Determination of the atomic oxygen chemical potential is straightforward:

$$\mu_{\mathrm{O}}(T, p_{O_2}) = \frac{1}{2} g_{O_2}(T) + \frac{1}{2} k_{\mathrm{B}} T \ln\left\{ \frac{p_{O_2}}{1 \text{ atm}} \right\}, \qquad (3)$$

where k_{B} is the Boltzmann constant and $g_{O_2}(T)$ is the standard Gibbs free energy of molecular oxygen at T and $p_{O_2} = 1$ atm; this is chosen so that at room temperature, $g_{O_2} = 0$ eV by definition, giving $\mu_{\mathrm{O}}^0 = 0$ eV as the upper bound on reasonable oxygen chemical potentials. Figure 2 illustrates the relationship between μ_{O} and (T, p_{O_2}), using experimental values of $g_{O_2}(T)$ obtained from Ref. 23.

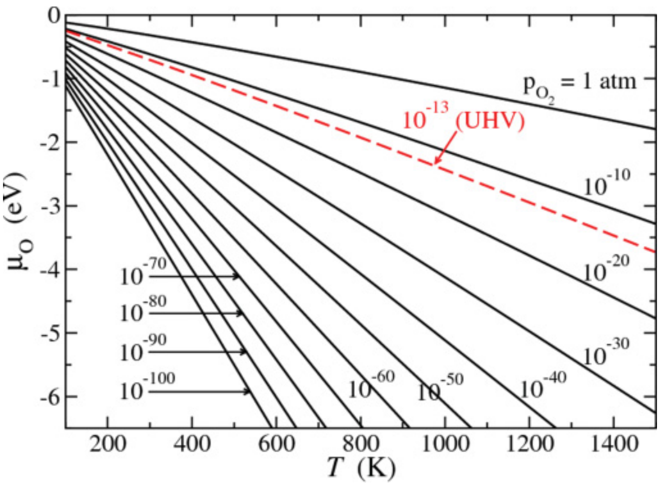

FIG. 2. (Color online) The oxygen chemical potential as a function of temperature at various oxygen partial pressures (in atm).

We assume that bulk $SrTiO_3$ is always in equilibrium (i.e., the interior of the oxide film is stable), so we can write the Ti chemical potential in terms of μ_{O} and μ_{Sr}:

$$\mu_{\mathrm{Ti}} = g_{\mathrm{SrTiO_3}}^{\mathrm{bulk}} - \mu_{\mathrm{Sr}} - 3\mu_{\mathrm{O}}, \qquad (4)$$

where $g_{\mathrm{SrTiO_3}}^{\mathrm{bulk}}$ is the free energy per formula unit of bulk $SrTiO_3$. Furthermore, we want $SrTiO_3$ to be the only bulk phase in the system (i.e., as per experiment, there is no undesired formation of bulk Sr, Ti, SrO, TiO_2, or other $Sr_xTi_yO_z$ phases), so the Sr, Ti, and O chemical potentials must be bound by the following constraints:

$$\mu_{\mathrm{Sr}} + \mu_{\mathrm{O}} \leqslant g_{\mathrm{SrO}}(T), \qquad (5)$$

$$\mu_{\mathrm{Sr}} \leqslant g_{\mathrm{Sr}}(T), \qquad (6)$$

$$\mu_{\mathrm{Ti}} + 2\mu_{\mathrm{O}} \leqslant g_{\mathrm{TiO_2}}(T), \qquad (7)$$

$$2\mu_{\mathrm{Ti}} + 3\mu_{\mathrm{O}} \leqslant g_{\mathrm{Ti_2O_3}}(T), \qquad (8)$$

$$\mu_{\mathrm{Ti}} + \mu_{\mathrm{O}} \leqslant g_{\mathrm{TiO}}(T), \qquad (9)$$

and

$$\mu_{\mathrm{Ti}} \leqslant g_{\mathrm{Ti}}(T). \qquad (10)$$

To accurately relate the experimentally derived phase boundaries to our DFT results, we set the zero-temperature value of the bulk Gibbs free energy for each bulk phase to equal the DFT-computed bulk formation energy. Table I shows that the DFT values for the bulk formation energies are in reasonable agreement with experiment.

TABLE I. Bulk formation energies in eV per formula unit. The $SrTiO_3$ formation energy is with respect to bulk SrO and TiO_2; others are with respect to the constituent elements in their standard states. The corrected O_2 energy is used.[38] The experimental formation enthalpies are at $T = 300$ K.

	DFT-GGA, present	DFT-GGA, previous	Experiment
SrO (rocksalt)	−5.87	−5.50 (Ref. 24)	−6.14 (Ref. 23)
TiO_2 (rutile)	−9.83	−10.14 (Ref. 25)	−9.73 (Ref. 23)
Ti_2O_3 (corundum)	−15.63	−16.30 (Ref. 25)	−15.76 (Ref. 23)
TiO (rocksalt)	−4.98	−5.30 (Ref. 25)	−5.62 (Ref. 23)
$SrTiO_3$ (cubic)	−1.19	−1.23 (Ref. 26)	−1.4 (Ref. 27)
SiO_2 (crystabolite)	−9.02		−9.39 (Ref. 23)

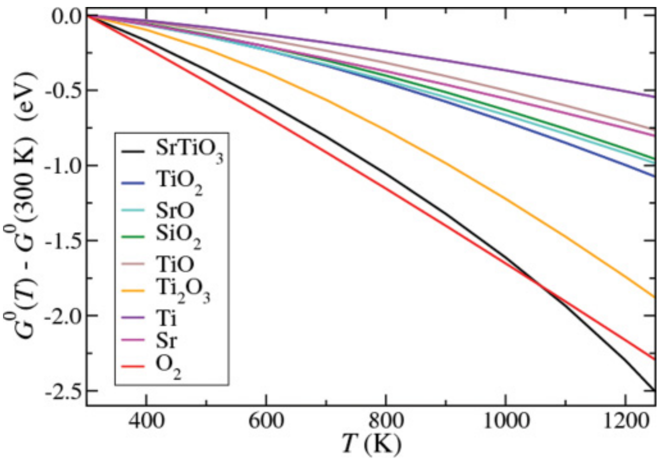

FIG. 3. (Color online) Experimental Gibbs free energy as a function of temperature for various materials. The data for the elemental and binary compounds are obtained from Ref. 23. The $SrTiO_3$ data are from Ref. 27.

The constraints of Eqs. (5)–(10) include the temperature dependences of the bulk Gibbs free energies g_i. Neglecting these dependences can have a significant effect, as the temperature dependence of the free energy is a material-dependent property; this is illustrated for the materials relevant to the $SrTiO_3$/Si system in Fig. 3. Consequently, the region of phase space in which bulk $SrTiO_3$ is stable as a single phase is also temperature dependent; as mentioned in Ref. 28, the correct definition of the stability region can be essential for accurate prediction of experimental surface and interface structures using the *ab initio* thermodynamics approach.

Equations (4)–(10) delineate the region in (μ_{Sr},μ_{Ti},μ_O) phase space in which bulk $SrTiO_3$ is stable; thermodynamic equilibrium of the $SrTiO_3$/Si heterostructure requires the additional constraints that neither bulk SiO_2 nor any bulk strontium or titanium silicides are present. The former constraint turns out to be the most important in this system, enforcing a maximum oxygen chemical potential of

$$2\mu_O \leqslant 2\mu_O^{\max} = g_{SiO_2}(T) - \mu_{Si}. \qquad (11)$$

At room temperature, $\mu_O^{\max} \approx -4.77$ eV ($\mu_{Si} = 0$ by definition since the substrate provides a reservoir of bulk silicon). Examination of Fig. 2 shows that this value corresponds to an oxygen partial pressure $p_{O_2} \approx 10^{-60}$ atm at $T = 873$ K, the highest temperature encountered during the growth procedure. Experimentally, such low oxygen partial pressures are inaccessible: typical ultrahigh-vacuum (UHV) pressures are $\sim 10^{-13}$ atm. Consequently, under all reasonable growth conditions, SiO_2 formation is thermodynamically favored. In other words, there should, at equilibrium, always be a region of amorphous SiO_2 at the $SrTiO_3$/Si interface.

It is evident that no thermodynamically stable, atomically abrupt $SrTiO_3$/Si heterostructure can be obtained using current growth techniques. Thus, the experimentally demonstrated and successful growth of epitaxial $SrTiO_3$ on silicon is *only* possible due to the kinetic inhibition of bulk SiO_2 formation at the interface. We discuss the mechanism for this inhibition—and the implications of this conclusion for predicting the interface atomic structure via first-principles DFT computations—in Sec. IV.

III. THE $SrTiO_3$/Si PHASE DIAGRAM

The computed thermodynamic phase diagram of the $SrTiO_3$/Si heterostructure is presented in Fig. 4, which shows the most stable of the 56 interface compositions in the (μ_O,μ_{Sr}) phase space [μ_{Ti} is constrained by the equilibrium of bulk $SrTiO_3$, Eq. (4)]. The atomic structures of the most stable interface composition in each of the key regions in the (μ_O,μ_{Sr}) phase space are illustrated in Fig. 5. Under experimental growth conditions, the most stable atomically abrupt interface structure is composed of 1/2 monolayer

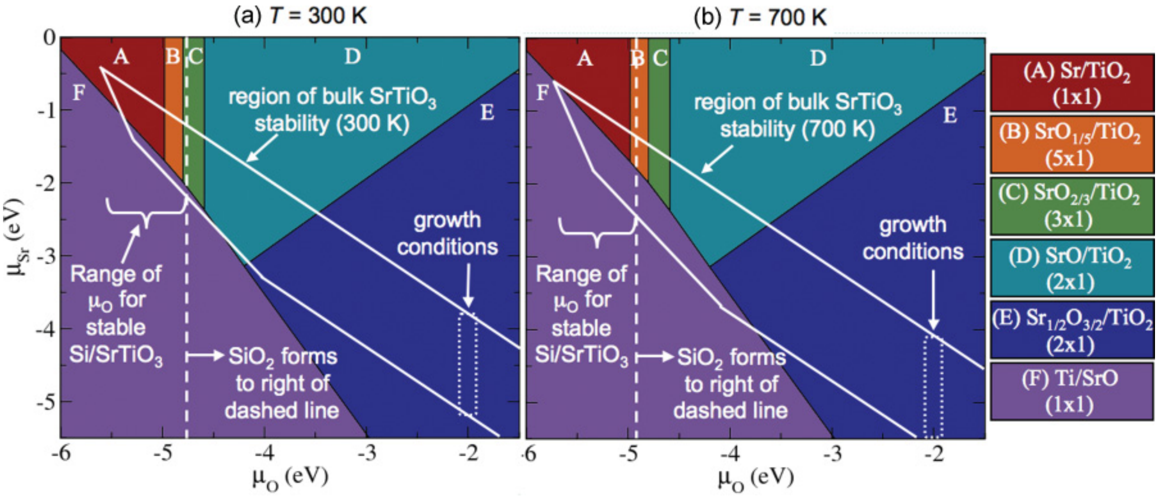

FIG. 4. (Color online) The computed $SrTiO_3$/Si interface phase diagram as a function of oxygen and strontium chemical potentials ($\mu_{Ti} = g_{SrTiO_3} - \mu_{Sr} - 3\mu_O$). The white lines indicate the boundaries of bulk $SrTiO_3$ stability at (a) $T = 300$ K and (b) $T = 700$ K. For each temperature, the vertical white dashed line shows the upper bound on μ_O given by the constraint that no bulk SiO_2 is present in the system; interface phases to the right of the dashed line are therefore thermodynamically unstable with respect to formation of an interfacial region of bulklike SiO_2.

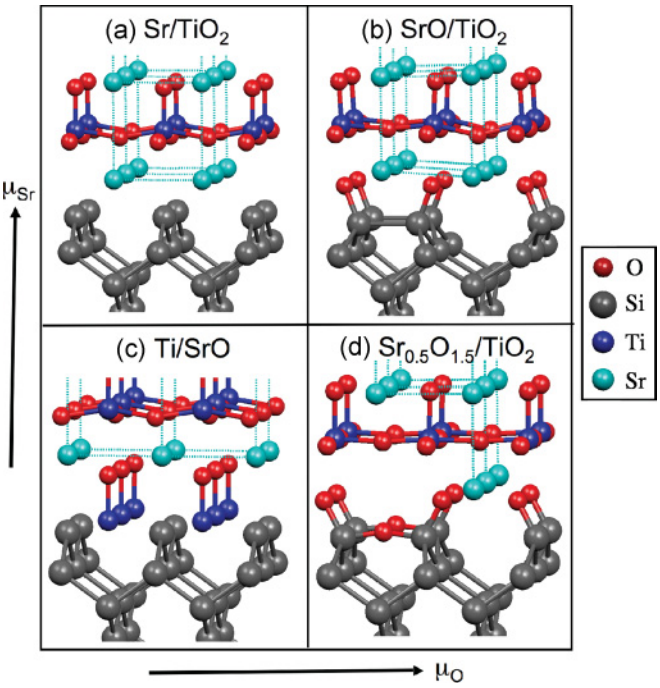

FIG. 5. (Color online) Relaxed atomic structures for the most stable $SrTiO_3$ interface compositions under (a) O-poor, Sr-rich, (b) O-rich, Sr-rich, (c) O-poor, Sr-poor, and (d) O-rich, Sr-poor conditions. The phases between the O-poor, Sr-rich and the O-rich, Sr-rich phases are locally similar to the two extremes, but with varying interfacial oxygen concentrations. Both O-rich structures (b) and (d) are thermodynamically unstable with respect to the formation of a bulklike SiO_2 region.

(ML) Sr and 3/2 ML O between the Si substrate and a TiO_2-terminated $SrTiO_3$ film [Fig. 5(d)]. However, as the phase diagram indicates, this interface is not thermodynamically stable with respect to formation of SiO_2. This is also the case for the phase illustrated in Fig. 5(b). In general, once oxygen enters the interface and Si-O bonds are formed, the structure is thermodynamically unstable with respect to bulk SiO_2 formation: i.e., the heterostructure will lower its free energy by $(1/2)(g_{SiO_2} - 2\mu_O)$ for every oxygen atom that moves from the reservoir through the interface and into the bulk substrate to form a unit cell of SiO_2. At constant μ_O, this process will in principle continue until the entire silicon substrate is oxidized to SiO_2, although in practice the extent of the oxidation, and thus the thickness of the interfacial SiO_2 layer, is governed by the rate of oxygen diffusion, a subject we return to later.

Figure 4 clearly illustrates that the region in which the $SrTiO_3$/Si heterostructure *is* thermodynamically stable (i.e., bulk $SrTiO_3$ is stable but bulk SiO_2 is not) encompasses a small area in the low-μ_O, high-μ_{Sr} corner of the phase diagram. Theoretically, most of the thermodynamically stable interfaces thus have a full monolayer of Sr and little or no oxygen in the interface layer [Fig. 5(a)]. The one exception is the O-poor, Sr-poor region of the diagram (i.e., the Ti-rich region) which can in principle be accessed at higher temperatures, as indicated by its inclusion within the white boundaries in Fig. 4(b). However, this phase is characterized by a full ML of Ti at the interface, as shown in Fig. 5(c), and is not expected to form experimentally: as we discuss below, the experimental growth is performed with a Sr:Ti ratio greater than 1 so that the system is always in the high-μ_{Sr} regime and closer to the $SrTiO_3$-SrO equilibrium boundary (upper white boundary) than to the bulk $SrTiO_3$-TiO_2 equilibrium (lower white boundary). Furthermore, the Ti-rich phase is unstable with respect to formation of undesirable (and unobserved) $TiSi_2$.

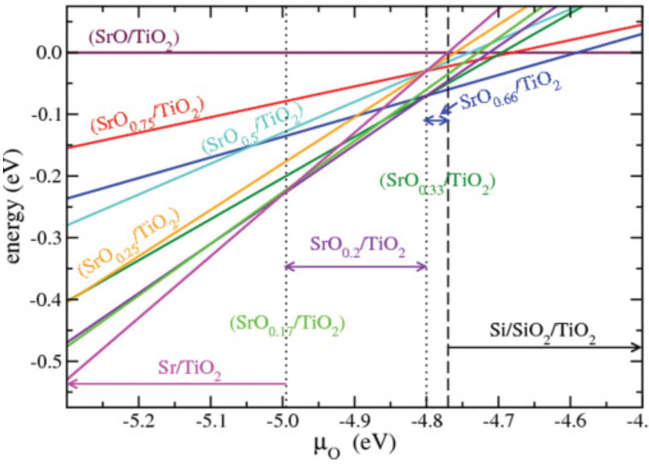

FIG. 6. (Color online) Free energy vs μ_{O_2} for structures with 1 ML Sr and varying interfacial oxygen concentration. For convenience, the Sr and Ti chemical potentials are set to zero (the structures have the same number of Sr and Ti atoms). The zero of energy is set to be the free energy of the structure with a full ML of O at the interface (i.e., one interfacial O per Si). The vertical dashed line shows the oxygen chemical potential above which SiO_2 formation is thermodynamically favored. The vertical dotted lines indicate the boundaries between different interface phases; the phases labeled with parentheses across the boundary lines coexist with the two phases on either side of the boundary under a very small range of m_O.

As one moves in the direction of increasing μ_O from the lowest-μ_O structure [the structure in Fig. 5(a) and region A in Fig. 4], along a path within the boundaries for $SrTiO_3$ stability, the thermodynamically stable interface structure evolves in a straightforward manner, with the oxygen concentration at the interface increasing with μ_O (regions B and C in Fig. 4); once the oxygen concentration is greater than ≈2/3, the interface becomes unstable to SiO_2 formation. While we find that several particular interfacial oxygen concentrations are thermodynamically stable (and thus appear in Fig. 4), all possible oxygen concentrations cannot realistically be explored via DFT. However, Fig. 6 shows that the difference in the free energy of the various phases in this region is quite small; physically, this means that one might expect the transitions between the main phases on the diagram in Fig. 4 to be "blurred," as the interface oxygen concentration changes more or less continuously. In addition, these results suggest that entropic effects will lead to a random distribution of interfacial oxygen at low oxygen concentrations, which would manifest experimentally as a 1 × 1 symmetry in diffraction-based characterization methods.

As discussed above, the heterostructure without SiO_2 is thermodynamically stable only in the regime of inaccessibly low oxygen partial pressures, leading to the conclusion that the experimentally observed interface structure is kinetically trapped. One might therefore ask, why compute the thermodynamic phase diagram at all? Clearly, *ab initio* thermodynamics alone is not adequate to predict the experimental structure.

Nevertheless, the equilibrium phase diagram provides important information about the system which can be used to infer the structure of kinetically trapped states. For example, Fig. 4 shows that all but one of the interface phases present in the diagram belong to the class of structures with a TiO_2 plane adjacent to the interface layer, suggesting that the interaction between the the silicon substrate and the TiO_2 plane plays a significantly role in stabilizing the heterostructure. As a result, we may reasonably expect the experimental structure to have this feature.

Furthermore, the lack of an interfacial SiO_2 layer implies that the structure is not in equilibrium with oxygen. Intuitively, the inhibition of oxygen diffusion will make the "local" oxygen chemical potential at the interface much lower than the oxygen chemical potential in the growth chamber: one may then expect the interface to be trapped in a structure that corresponds to a thermodynamically stable one for low oxygen chemical potential. This physical picture also points us toward the pathways that lead to equilibrium and thus the kinetic mechanisms that we will analyze in the next section.

IV. NONEQUILIBRIUM STRUCTURE PREDICTION

The above analysis shows that, at any temperature, accessing the equilibrium $SrTiO_3$/Si interface phases in the region for which $SrTiO_3$ is thermodynamically stable but SiO_2 is not requires an unphysically low oxygen partial pressure. Hence, the experimentally observed, atomically abrupt interface must be a kinetically trapped structure. In itself, this is not surprising, as the interface can only be grown via a specialized procedure[29] that inhibits the formation of amorphous SiO_2 at the interface and operates within a relatively narrow range of parameters. Given the large thermodynamic driving force toward SiO_2 formation and the high mobility of oxygen in bulk $SrTiO_3$, however, it is surprising that, regardless of how the structure is trapped in the initial growth steps, it does not form SiO_2 during later growth steps that are performed at high temperatures. Nor does an SiO_2 interface layer form after the sample has been removed from the growth chamber and kept at ambient conditions for months or even years. By this we mean that the experimentally measured rates of oxygen incorporation[30,31] and diffusion[31–33] in bulk $SrTiO_3$ under ambient conditions suggest that the system should reach equilibrium in a reasonable time period. What prevents the system from evolving to its equilibrium state and thus enables the growth of epitaxial $SrTiO_3$/Si? We answer this question in the following subsections, in which we develop a DFT-based model to predict the kinetically trapped structure.

A. Experimental growth procedure

We begin with the experimental growth procedure outlined in Table II.The initial half monolayer of Sr is deposited onto a clean silicon substrate with an ordered Si-dimer surface[34] and no amorphous SiO_2 layer, as indicated by a strong 2 × 1 reflection high-energy electron diffraction (RHEED) pattern.[35] During this step, the Si does not reach equilibrium with O_2: assuming ideal gas behavior, the number of O_2 collisions that occur during the 30 s Sr deposition is approximately one O_2 molecule per 1000 surface unit cells. It is not possible to form a significant fraction of a monolayer of oxygen during the first step: typical oxygen sticking probabilities to the surface[36] are small, indicating that the oxygen coverage after the first step will be far lower than 10^{-3}. Table II shows that the O_2 content remains below equilibrium during the second step as well. Although the number of collisions increases significantly with the increase in the oxygen partial pressure in steps 3 and 4, given the O_2 sticking probability, it is reasonable to assume that the structure remains oxygen poor during these steps (i.e., most oxygen binding sites are unoccupied).

Nevertheless, given the elevated temperature and the duration of step 6, one would expect the system to approach equilibrium. Oxygen diffusion via oxygen vacancies in bulk $SrTiO_3$ is rapid, with a diffusion coefficient of $D_0 \approx 10^{-12}$ cm^2 s^{-1} at room temperature.[31–33] The average time for an oxygen vacancy to diffuse across the film under ambient conditions is thus

$$t \approx \frac{l^2}{2D_0} = 0.02 \text{ s}, \tag{12}$$

where the root-mean-square distance traveled is the film thickness $l \approx 2$ nm or five unit cells. Therefore, even though the interface is initially oxygen poor, the oxygen in the heterostructure will rapidly reach thermodynamic equilibrium under ambient conditions—unless something about the interface

TABLE II. Summary of key experimental growth parameters for $SrTiO_3/Si$.[35] The collision rates are estimated using the ideal gas law.

Step	Deposition	T (K)	p_{O_2} (atm)	t (min)	No. O_2 collisions (per 2D unit cell)
1	$\frac{1}{2}$ ML Sr	873	10^{-13}	0.5	3×10^{-3}
2	$\frac{1}{2}$ ML Sr	373	10^{-13}	0.5	4.8×10^{-3}
3	$\frac{1}{2}$ ML Sr	373	10^{-10}	0.5	4.8
4	Oxidize	373	10^{-10}	0.5	4.8
5	$\frac{3}{2}$ ML Sr + 2 ML Ti	373	10^{-10}	3.5	16.8
6	Recrystallize	673	10^{-10}	10	36
7	1:1 Sr and Ti	673	10^{-10}	1 min/layer	3.6/layer
	Ambient	300	1	—	1×10^9 s^{-1}

inhibits oxygen diffusion into the silicon substrate. Next, we consider the diffusion process in more detail to pinpoint the bottleneck for oxygen diffusion in the $SrTiO_3$/Si heterostructure.

B. Pathway to equilibrium

From the above analysis of the growth procedure, we can safely assume that the initial interface layer is oxygen poor. For simplicity, we will consider the initial structure to have no oxygen in the interface layer. (We show below that the results do not change if the initial structure has some interfacial oxygen.) To reach equilibrium, the system presumably must evolve through a structure with oxygen in the interface layer before the silicon interfacial region can be oxidized.

We first consider the process by which the O-poor, Sr-rich [Fig. 5(a)] structure evolves into the O-rich, Sr-rich structure [Fig. 5(b)], and we take the latter as our reference structure. In other words, we will use oxygen vacancies and their dynamics as the main variable in our analysis. Therefore, the reference structure has no oxygen vacancies, the O-poor Sr-rich structure has a full ML of vacancies, the next structure on the right on the phase diagram (Fig. 4) is missing four out of five oxygens in the interface layer, etc.

In order for an oxygen vacancy to disappear from the system, the oxygen vacancy must diffuse to the surface that is in contact with the atmosphere. The process can be considered as a chain of jumps: first an oxygen atom in the initial oxide layer fills the interface oxygen vacancy; now the vacancy is in the first layer, and an oxygen from the second atomic plane can fill it, resulting in the diffusion of the oxygen vacancy to the second layer, and so on, until the oxygen vacancy reaches the surface, or

$$V_{O,0} \underset{k_{-1}}{\overset{k_1}{\rightleftharpoons}} V_{O,1} \underset{k_{-2}}{\overset{k_2}{\rightleftharpoons}} V_{O,2} \cdots \underset{k_{-i}}{\overset{k_i}{\rightleftharpoons}} V_{O,i} \cdots \underset{k_{-n}}{\overset{k_n}{\rightleftharpoons}} V_{O,n}, \tag{13}$$

where $V_{O,i}$ represents an oxygen vacancy in the atomic plane i, and $i = 0$ and $i = n$ correspond to the interface and the surface, respectively. The forward and backward rate constants, k_i and k_{-i}, respectively, describe the diffusion of an oxygen vacancy from layer $i - 1$ to layer i and from layer i to layer $i - 1$, respectively. They are given by

$$k_i = \nu_i \exp(-E_{a,i}/k_B T), \tag{14}$$

where $E_{a,i}$ is the energy barrier for an oxygen vacancy to hop between layers, ν_i is the attempt frequency, and k_B is the Boltzmann constant.

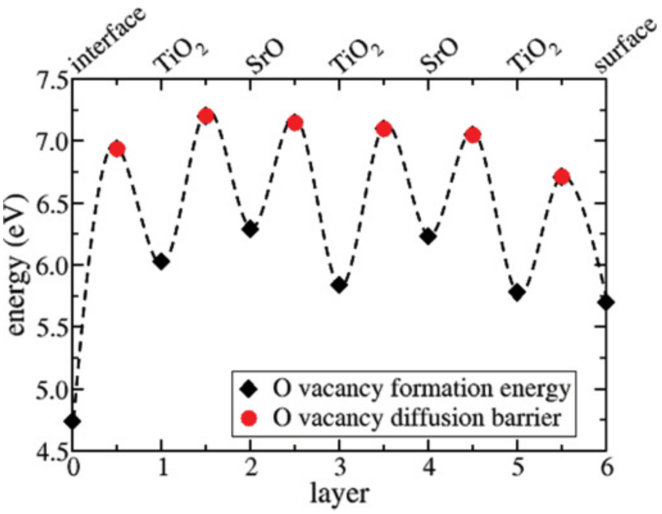

FIG. 7. (Color online) DFT-computed oxygen vacancy formation energies (diamonds) and diffusion barriers (circles) for each atomic plane in a three-unit-cell-thick film. The values, which are computed with a 2 × 1 in-plane supercell ($\theta = 1/2$ in Fig. 8), are also reported in Table III.

Once at the surface, the oxygen vacancy can be filled from the reservoir of oxygen gas. The process by which oxygen incorporation occurs is complex,[31] involving the adsorption of an oxygen molecule to the surface, dissociation into two neutral oxygen atoms on the surface, a charge transfer reaction to ionize the adsorbed oxygens to O^{2-}, diffusion over the surface to an oxygen vacancy site, and, finally, filling of the oxygen vacancy. Separating the time scale of these steps experimentally is quite challenging, but luckily it is also not relevant to our analysis: the experimental measurements give an overall effective reaction constant for the process, allowing us to consider the simplified reaction

$$V_{O,n} + \tfrac{1}{2}O_2(g) \rightleftharpoons k_{\text{fill}} X_{O,n}, \tag{15}$$

where X_O represents an occupied oxygen site in the perovskite lattice. Here, k_{fill} is taken from experiment, and has the following temperature and pressure dependence:[30]

$$k_{\text{fill}} = (4 \times 10^6\ \text{atm}^{-1}) p_{O_2} \exp(-1.35\ \text{eV}/k_B T)\ (\text{s}^{-1}). \tag{16}$$

C. Energy landscape for oxygen vacancies

Figure 7 and Table III show the energy required to form an oxygen vacancy in the $SrTiO_3$/Si heterostructure as a function of the vacancy position in the $SrTiO_3$ film. Interestingly, it costs ≈1.0–1.3 eV less energy to form an oxygen vacancy in the interface layer than elsewhere in the film. This means that once an oxygen vacancy is present at the interface, *there is no local driving force* for the vacancy to diffuse away from the interface; in fact, doing so requires moving significantly *uphill* in the energy landscape. Therefore, despite the fact

TABLE III. Values of the oxygen vacancy formation energies $\Delta E_{f,i}$ and diffusion barriers $E_{a,i}$ shown in Fig. 7. Barriers are for vacancy diffusion directed from the interface ($i = 0$) toward the surface ($i = 6$).

i	$\Delta E_{f,i}$	$E_{a,i}$
0	4.74	2.20
1	6.03	1.17
2	6.29	0.86
3	5.84	1.30
4	6.21	0.85
5	5.78	0.93
6	5.70	–

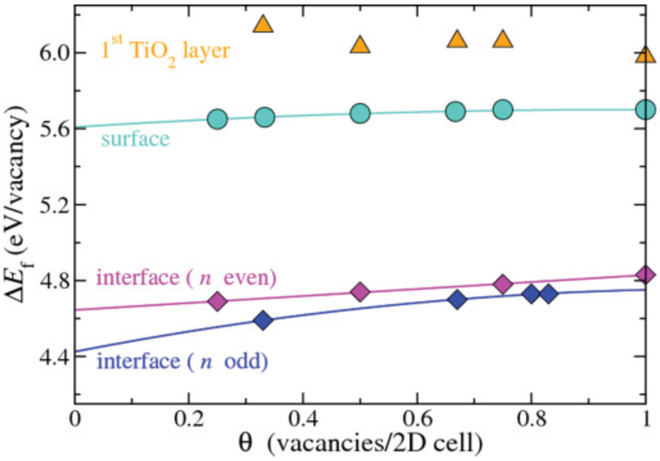

.

FIG. 8. (Color online) Formation energy ΔE_f per oxygen vacancy as a function of areal density at the film surface (circles), in the first oxide layer (triangles), and in the interface layer (diamonds). $n = 1/\theta$ is the number of unit cells in the x direction of the $n \times 1$ supercell; tests with $n \times n$ supercells indicate that the formation energy at a given θ is essentially independent of the arrangement of vacancies, i.e., the coupling between vacancies is very weak.

that the overall process of oxygen vacancy diffusion to the surface and incorporation of oxygen from the atmosphere is thermodynamically favorable, it is very unlikely to occur. From an alternate perspective, as long as there are oxygen vacancies present in the $SrTiO_3$ film, any oxygen in the interface layer will lower its energy by diffusing into the film.

Our finding that the most favorable position for an oxygen vacancy in the $SrTiO_3$/Si heterostructure is at the interface is independent of the arrangement of the vacancies within the interfacial plane (i.e., square lattice vs stripes), as well as the interfacial oxygen vacancy concentration, as demonstrated in Fig. 8. Figure 8 also shows that (i) oxygen vacancy formation is slightly more favorable at the surface than in the center of the film, which is expected since the removal of a surface oxygen atom results in fewer broken Ti-O bonds, and (ii) that vacancies located in SrO planes are more costly than those located in TiO_2 planes due to the tetragonal symmetry of the strained $SrTiO_3$ unit cell. (We find that the same is true for bulk $SrTiO_3$ with compressive in-plane strain.)

The dramatic position dependence of the oxygen vacancy formation energy reflects the difference in local chemistry between the interface and the interior of the $SrTiO_3$ film. The oxygens in these heterostructures are the most electronegative elements and hence, as expected, adopt a configuration close to O^{2-}. Removing a neutral oxygen atom then leaves two electrons per vacancy that fill available low-energy electronic states—the nature of which depends on the local chemistry.

Figure 9 compares local densities of states for the fully oxygenated reference system (center) to the same system with an oxygen vacancy in the interface layer (left) or in the first oxide plane (right). When the vacancy is in the oxide layer, we see a large perturbation in the electronic states in the band gap of the oxide whereby cation states dominated by Ti appear in the spectrum: these are essentially $SrTiO_3$ states with conduction band edge (i.e., Ti d) character that are filled by the electrons from the vacancy. (Oxygen vacancies in atomic planes further from the interface show similar behavior.)

In contrast, when the vacancy is in the interface layer, the main change in the electronic spectrum is the appearance of low-energy states in the interfacial Si layer. These states, which

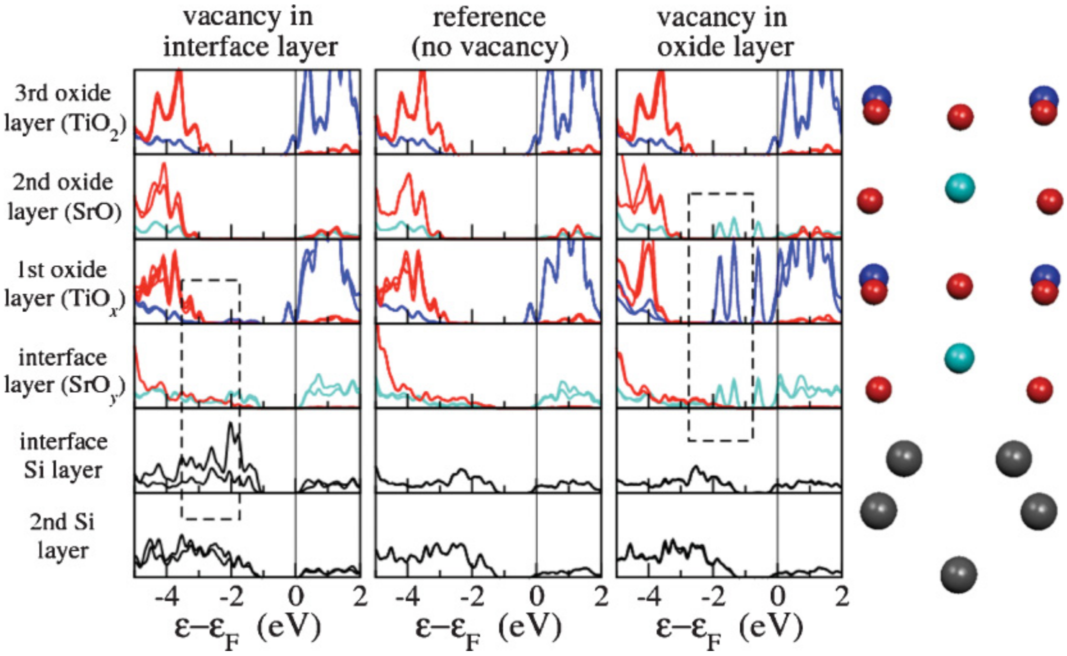

FIG. 9. (Color online) Atom-projected density of states (DOS) for structures with an oxygen vacancy in the interface layer (left) and initial oxide layer (right). The center panel shows the DOS for the reference structure with no oxygen vacancies [far right and Fig. 5(b)]. Black, cyan, blue, and red curves are for Si, Sr, Ti, and O atoms, respectively. The dashed boxes indicate the defect states, the character and energy levels of which depend on the position of the vacancy relative to the interface.

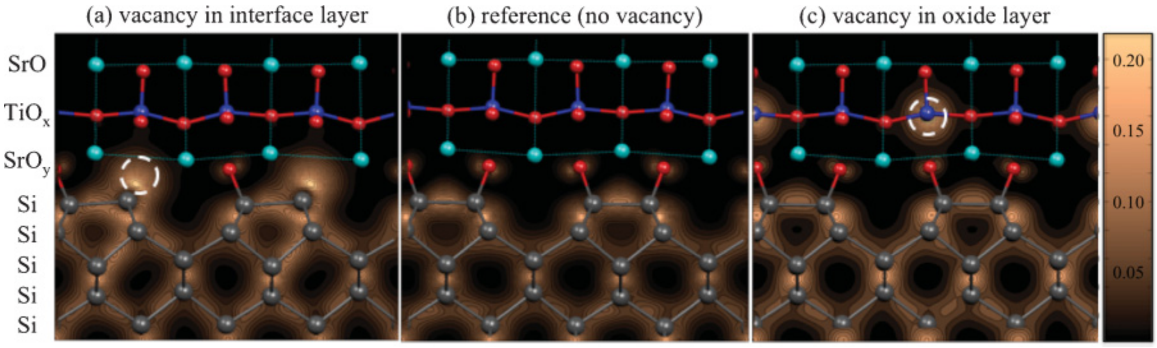

FIG. 10. (Color online) Integrated local density of states within the $SrTiO_3$ band gap, illustrating the spatial distribution of the oxygen vacancy defect states for oxygen vacancies in the initial oxide and interface layers [(a) and (c), respectively]. The vacancy positions are indicated by dashed circles.

correspond to the now available dangling bond state of the surface Si atom (that no longer has an oxygen neighbor), are filled by the donated electrons. The critical difference is that the Si dangling bond state is significantly lower in energy than the cation-derived states. The vacancy-donated electrons are therefore much more stable in the former state, significantly decreasing the formation energy of the vacancy. For a precise spatial visualization, Fig. 10 shows the integrated local densities of states for the above three cases over an energy window within the $SrTiO_3$ band gap (i.e., approximately within the dashed boxes in Fig. 9). The figure clearly shows the Si dangling bond state (left) and the defect states localized on the Ti (right).

D. Kinetic modeling

Our DFT results strongly suggest that there is a low probability for oxygen to diffuse to the interface. We now determine the probability for such events, the distribution of oxygen vacancies over time, and the time scale for oxygen incorporation into the $SrTiO_3$/Si heterostructure from the computed oxygen vacancy energies and diffusion barriers given in Fig. 7 and Table III.

To do so, we consider the reactions in Eqs. (13) and (15) for a three-unit-cell-thick $SrTiO_3$ film (six atomic layers). Combining and rewriting Eqs. (13) and (15) in matrix form gives the linear matrix equation

$$\frac{dc_i(t)}{dt} = \sum_{j=0}^{6} M_{ij} c_i(t)$$

for the oxygen vacancy concentration $c_i(t)$ in atomic plane i, where the matrix of rate constants M is

$$M = \begin{pmatrix} -k_1 & k_{-1} & 0 & 0 & 0 & 0 & 0 \\ k_1 & -k_{-1}-k_2 & k_{-2} & 0 & 0 & 0 & 0 \\ 0 & k_2 & -k_{-2}-k_3 & k_{-3} & 0 & 0 & 0 \\ 0 & 0 & k_3 & -k_{-3}-k_4 & k_{-4} & 0 & 0 \\ 0 & 0 & 0 & k_4 & -k_{-4}-k_5 & k_{-5} & 0 \\ 0 & 0 & 0 & 0 & k_5 & -k_{-5}-k_6 & k_{-6} \\ 0 & 0 & 0 & 0 & 0 & k_6 & -k_{-6}-k_{\text{fill}} \end{pmatrix}.$$

Here, $k_{\pm i}$ are the forward and backward rate constants for oxygen vacancy hopping to and from layer i [Eq. (14)]. The time-dependent oxygen vacancy concentrations are then easily found by finding the eigendecomposition of M and matching initial conditions. We note that the total number of oxygen vacancies in the interface and film is not conserved because vacancies are filled from the reservoir of O_2 gas at a rate k_{fill} [Eq. (16)]. Since the equilibrium state is a fully oxidized film and interface, the total vacancy number eventually decays to zero over a time scale dependent on the temperature and oxygen partial pressure via the rate constants in Eqs. (14) and (16).

To generate numerical results, we assume that the attempt frequencies ν_i in Eq. (14) all equal to the frequency of the Ti-O stretching mode in bulk $SrTiO_3$ ($\approx 10^{13}$ s^{-1}, independent of temperature[37,38]); that the initial condition has a uniform distribution of vacancies in all layers i (due to the linear nature of the problem, all generic initial distributions have essentially the same behavior: the vacancies rapidly fill the interface layer); and that the activation energy barriers in Eq. (14) are those computed from first principles in Fig. 7. Figure 11 shows the change in the oxygen vacancy concentration in each atomic plane at 673 K, the temperature at which most of the growth procedure is performed. The fraction of oxygen vacancies on

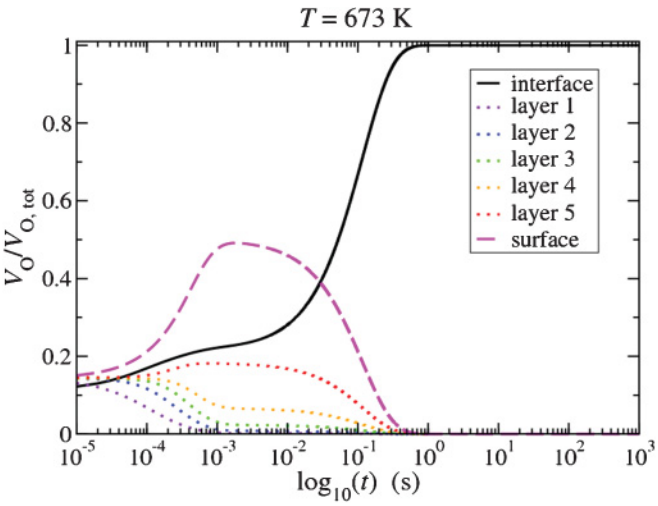

FIG. 11. (Color online) Distribution of oxygen vacancies in each atomic plane as a function of time at $T = 673$ K and $p_{O_2} = 1$ atm, starting from an initial homogeneous distribution. Over these time scales the total number of vacancies ($V_{O,tot}$) is essentially fixed, but over a much larger time $V_{O,tot}$ scales with the drop in total number. An estimate of the latter time ($\approx 6 \times 10^{10}$ s) is given in Table I; Fig. 12 shows a case where this behavior is visible.

the surface plane (dashed magenta curve) initially increases at very short time scales, but within a second the system rapidly reaches its quasiequilibrium state where essentially all the vacancies are at the interface layer (black curve). In other words, the vacancy distribution within the heterostructure is in equilibrium but has not reached equilibrium with the oxygen atmosphere. Figure 12 reveals that over a much longer time scale of $\sim 10^5$ s ($\sim$33 h), the vacancies are filled by oxygen from the atmosphere. At room temperature, it takes even longer for the system to reach quasiequilibrium, much less to equilibrate with the atmosphere. Thus, the structure obtained during the higher-temperature growth is frozen in under ambient conditions.

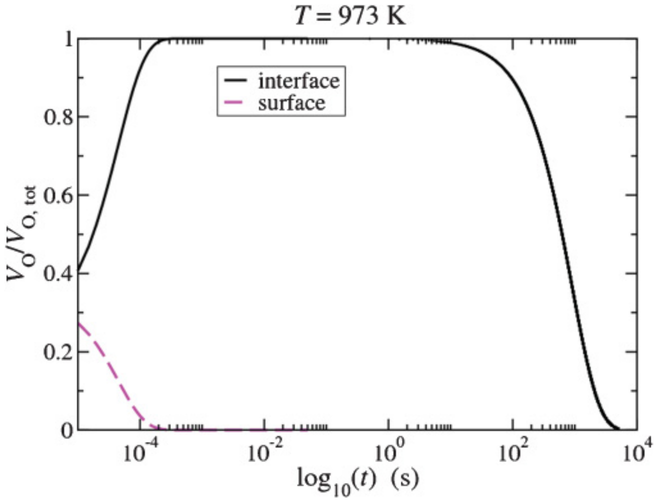

FIG. 12. Distribution of oxygen vacancies in the interface and surface planes as a function of time at $T = 973$ K and $p_{O_2} = 1$ atm, illustrating the short time scale for the system to evolve from the initial homogeneous state to the metastable state in which all oxygen vacancies are located in the interface layer, and the much longer time scale over which all of the oxygen vacancies in the film are filled from the atmosphere.

Going to a higher temperature of 973 K, the behavior is qualitatively similar, with the fraction of oxygen vacancies in the surface layer initially increasing, then decreasing rapidly to zero as all of the vacancies diffuse to the interface (Fig. 12). However, the time required for the system to equilibrate with the O_2 atmosphere is much shorter at this temperature: after $\approx$1000 s ($\approx$16 min), roughly half of the oxygen vacancies are filled.

Since there are two very different time scales governing the system, we can easily model the overall approach to equilibrium using only the total number of oxygen vacancies $N_{tot}(t)$ as the variable. The system reaches quasiequilibrium rapidly, typically within a second, at fixed $N_{tot}(t)$ with almost all vacancies going to the interface; then rarely a vacancy wanders to the surface where it can be filled (i.e., disappear). This means that we have the Boltzmann distribution for oxygen vacancy distribution at fixed $N_{tot}(t)$ given by

$$\frac{N_i}{N_{tot}} = \frac{\exp\left(-E_f^i/k_B T\right)}{\sum_{i=0}^{n}\exp\left(-E_f^i/k_B T\right)}, \tag{17}$$

where i labels the atomic planes in the $SrTiO_3$ film, $i = 0$ and $i = n$ correspond to the interface and surface atomic planes, respectively, and E_f^i are the computed oxygen vacancy formation energies for a vacancy in plane i (Table III). The change in $N_{tot}(t)$ occurs at the surface and is given by

$$\frac{dN_{tot}(t)}{dt} = -k_{fill} f_{surf} N_{tot}(t), \tag{18}$$

where $f_{surf} = N_n/N_{tot} = N_{surf}/N_{tot}$ is the (essentially) time-independent fraction of the total number of oxygen vacancies located on the film surface [Eq. (17)] and k_{fill} is the rate of surface oxygen incorporation given in Eq. (16). Solving Eq. (18) gives

$$N_{tot}(t) = N_{tot}(0)\exp(-k_{fill} f_{surf} t).$$

The time required to fill half of the oxygen vacancies is thus

$$t_{1/2} = \frac{\ln 2}{k_{fill} f_{surf}}. \tag{19}$$

Values of $t_{1/2}$ and other key parameters are compiled in Table IV for a few relevant temperatures. Only at $T = 1273$ K does the rate of oxygen incorporation become comparable to that of film growth. Since the film is not exposed to such high temperatures, no decrease in the net oxygen vacancy concentration will occur during the growth, and no oxygen vacancies will be filled from the atmosphere under ambient conditions.

E. Interface structure prediction

As we discussed in Sec. IV A, oxygen incorporation is prevented in the first steps of the growth procedure, leading to an initially oxygen-poor structure. Due to the intrinsic properties of the interface, oxygen vacancies are significantly more stable at the interface compared to anywhere else in the film; this feature, as well as large barriers to oxygen diffusion away from the interface, prevents achievement of thermodynamic

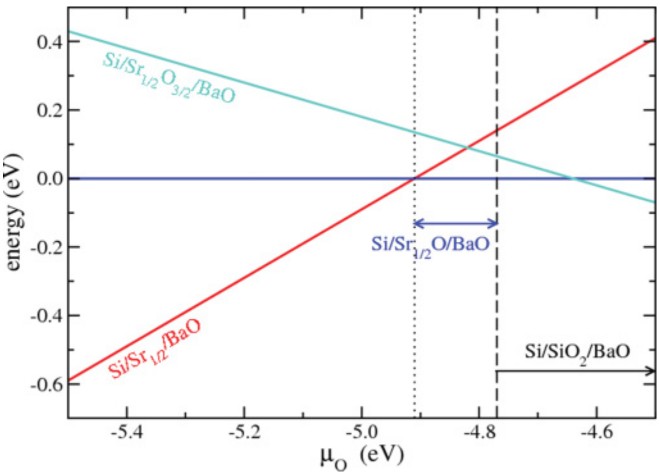

FIG. 13. (Color online) Gibbs free energy of BaO/Si interfaces as a function of oxygen chemical potential. The crossover in stability between the interfaces with and without oxygen occurs at $\mu_O < \mu_O^{max}$ (vertical dashed line), the chemical potential above which SiO$_2$ formation is thermodynamically favorable.

equilibrium on reasonable time scales. Consequently, once one or two atomic layers of SrTiO$_3$ are grown, the interface is stuck in the initial O-poor structure unless it is annealed at high temperatures or for very long times. Thus, the experimentally observed SrTiO$_3$/Si interface will have little or no oxygen and we can assume that the structure corresponds to the equilibrium structure predicted for very low oxygen chemical potential. In other words, the "local" oxygen chemical potential at the interface is lower than the oxygen chemical potential at which SiO$_2$ formation becomes favorable.

Examination of the phase diagram in Fig. 4 therefore indicates that the experimental structure will have a negligible interfacial oxygen concentration, 1×1 in-plane symmetry, and a TiO$_2$ plane adjacent to the interface layer. As discussed in Sec. III, a small concentration of oxygen at the interface is likely to be highly disordered, so that a 1×1 symmetry will be observed with diffraction-based experimental techniques. We therefore predict that the experimentally observed structure will, on average, be the O-poor, Sr-rich structure shown in Fig. 5(a), with no oxygen in the interface layer. We demonstrated previously[21] that this structure is in very good agreement with experimental characterization.

F. Comparison to BaO/Si

The above results suggest that there is no way to obtain a SrTiO$_3$/Si interface structure with an interface composition of Sr$_{1/2}$O and an initial SrO oxide plane—and thus no way to achieve the >1 eV conduction band offset required for transistor applications. The predicted interface structure has a very small conduction band offset and a large density of interface states,[39] both of which are detrimental for the envisioned applications. However, we found previously[3] that the experimental epitaxial BaO/Si structure is in fact analogous to the desired SrTiO$_3$/Si interface structure, begging the question of what is the difference between the two systems. Why doesn't BaO/Si, which has oxygen in the interface layer, further oxidize to form an amorphous SiO$_2$ layer?

TABLE IV. Key parameters describing the filling of oxygen vacancies from the oxygen gas atmosphere as a function of temperature. $t_{1/2}$ is the estimated time for half of the oxygen vacancies to be filled from Eq. (19), (N_{surf}/N_{tot}) from Eq. (18) is the fraction of the vacancies on the surface, and k_{fill} from Eq. (16) is the experimental rate at which vacancies are filled at the surface of SrTiO$_3$.

T (K)	N_{surf}/N_{tot}	k_{fill} (s^{-1})	$t_{1/2}$
300	2×10^{-17}	1×10^{-17}	10^{26} yr
673	3×10^{-8}	1×10^{-4}	2000 yr
973	7×10^{-6}	0.2	6 days
1273	1×10^{-4}	11	9 min

One reason for this difference is that the BaO/Si interface structure is thermodynamically stable at oxygen chemical potentials below that required for SiO$_2$ formation. In other words, the phase boundary between the oxidized and unoxidized interface structure is shifted to lower μ_O compared to that in the SrTiO$_3$/Si system, as illustrated in Fig. 13.This is primarily due to the different bonding interactions between the interface layer and the first oxide layer when the latter is BaO as opposed to TiO$_2$. Due to the geometry, a TiO$_2$ initial oxide layer is much closer to the substrate than an *A*O initial oxide layer (see Fig. 14 in the Appendix), leading to a significant overlap (i.e., bonding) between the Ti 3*d* orbitals and the interfacial Sr/Si states and increasing the stability of the oxygen-poor state.[39] For the same reason, the energetic preference for having an oxygen vacancy in the interface layer versus the first oxide layer is much smaller in BaO/Si (0.6 eV compared to 1.3 eV in SrTiO$_3$/Si), explaining why oxygen is able to diffuse to the interface in BaO/Si but not SrTiO$_3$/Si under the same initial growth conditions. However, the mechanism by which further oxygen diffusion into the silicon substrate is prevented in BaO/Si should be further explored, as it may suggest methods for trapping the analogous SrTiO$_3$/Si interface structure.

V. SUMMARY

We have computed the thermodynamic phase diagram of the epitaxial SrTiO$_3$/Si interface, demonstrating that no atomically abrupt interface structure is thermodynamically stable under attainable oxygen partial pressures. We have shown that in combination with experimental information, the computed phase diagram allows one to guess the most likely metastable structures and hypothesize a mechanism for the kinetic trapping. Using first-principles calculations and simple kinetic modeling, we have applied our understanding of the interface chemistry to describe a quantitative physical picture of how the interface gets trapped in the observed nonequilibrium structure, and why it does not evolve to thermodynamic equilibrium during growth or under ambient conditions. We have demonstrated that both phenomena are ultimately a consequence of the interface electronic structure, which provides preferential stability for oxygen vacancies in the interface layer and leads to a large kinetic barrier for vacancy diffusion away from the interface. Our results illustrate the key role of this barrier in enabling epitaxial growth of the SrTiO$_3$/Si heterostructure, and suggest possible

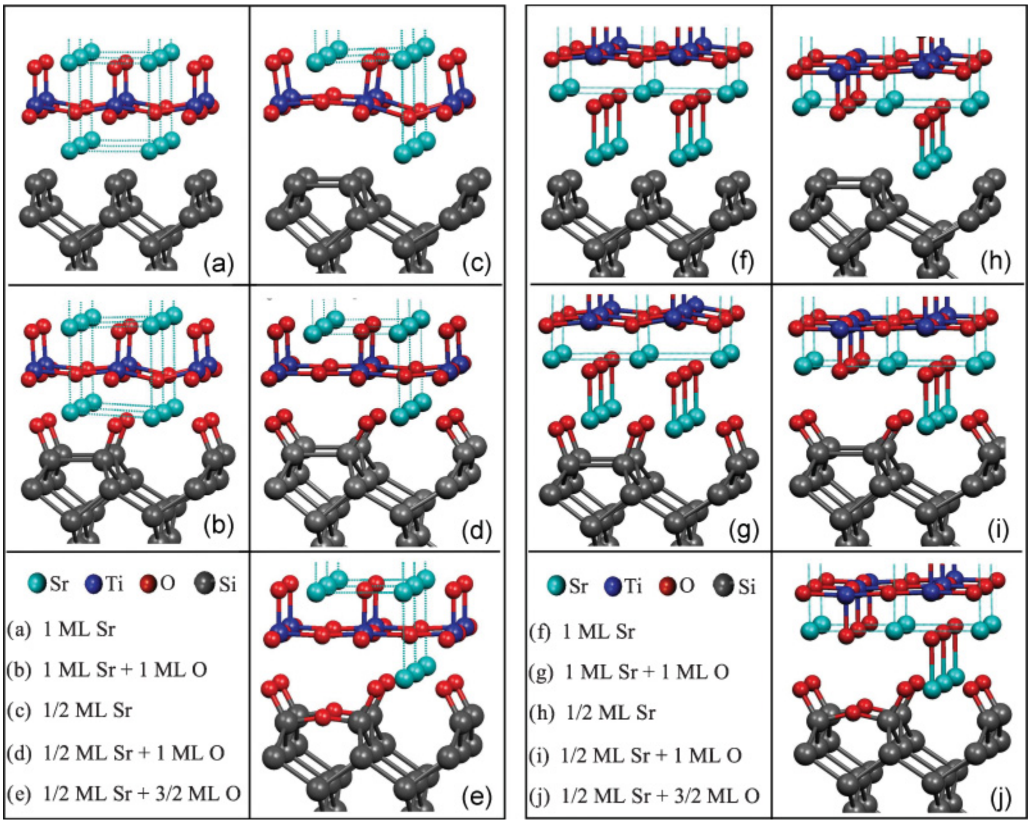

FIG. 14. (Color online) Relaxed interface structures for the representative interface compositions. Structures (a)–(e) have an initial TiO_2 layer, and structures (f)–(j) have an initial SrO layer, with direct, rocksaltlike bonds between the interfacial Sr and the oxygen in the SrO layer.

TABLE V. Representative structures for computation of the phase diagram. Column 1 indicates the composition of the interface layer (the atomic layer directly above the silicon); column 2 indicates the $SrTiO_3$ termination (the oxide plane adjacent to the interface layer). Column 3 refers to the corresponding panel in Fig. 14 illustrating the relaxed interface structure.

Interface layer	First oxide layer	Label	Reference
1 ML Sr	1 ML TiO_2	(a)	[41]
1 ML Sr, 1 ML O	1 ML TiO_2	(b)	[18–20]
$\frac{1}{2}$ ML Sr	1 ML TiO_2	(c)	
$\frac{1}{2}$ ML Sr, 1 ML O	1 ML TiO_2	(d)	[4,19]
$\frac{1}{2}$ ML Sr, $\frac{3}{2}$ ML O	1 ML TiO_2	(e)	
1 ML Sr	1 ML SrO	(f)	
1 ML Sr, 1 ML O	1 ML SrO	(g)	
$\frac{1}{2}$ ML Sr	1 ML SrO	(h)	[4,15]
$\frac{1}{2}$ ML Sr, 1 ML O	1 ML SrO	(i)	[4,15]
$\frac{1}{2}$ ML Sr, $\frac{3}{2}$ ML O	1 ML SrO	(j)	[4]

means for developing successful growth procedures for other epitaxial oxide/semiconductor heterointerfaces.

ACKNOWLEDGMENTS

We acknowledge support from the National Science Foundation under Grant No. MRSEC DMR 0520495, as well as computational support from the NCSA TeraGrid and Yale HPC. We thank J. W. Reiner, F. J. Walker, and C. H. Ahn for many fruitful discussions.

APPENDIX

We compute the minimum-energy structures for a total of 56 distinct interface compositions to determine the phase diagram shown in Fig. 4. This set includes but is not limited to all previously published structures.[2,4,15,17–20,40] Representative examples are illustrated in Fig. 14. Table V identifies each structure with the notation used in Ref. 21 and indicates work in which a similar structure has been proposed and/or studied.

---

[1] S. A. Chambers, Adv. Mater. **22**, 219 (2009).
[2] R. A. McKee, F. J. Walker, M. Buongiorno Nardelli, W. A. Shelton, and G. M. Stocks, Science **300**, 1726 (2003).
[3] Y. Segal, J. W. Reiner, A. M. Kolpak, Z. Zhang, S. Ismail-Beigi, C. H. Ahn, and F. J. Walker, Phys. Rev. Lett. **102**, 116101 (2009).

[4] P. W. Peacock and J. Robertson, Appl. Phys. Lett. **83**, 5497 (2003).
[5] C. S. Wang and W. E. Pickett, Phys. Rev. Lett. **51**, 597 (1983).
[6] K. Reuter and M. Scheffler, Phys. Rev. Lett. **90**, 046103 (2003).
[7] A. Pasquarello, M. S. Hybertsen, and R. Carr, Nature (London) **396**, 58 (1998).
[8] Y. Tu and J. Tersoff, Phys. Rev. Lett. **89**, 086102 (2002).
[9] J. W. Reiner, A. Posadas, M. Wang, M. Sidorov, Z. Krivokapic, F. J. Walker, T. P. Ma, and C. H. Ahn, J. Appl. Phys. **105**, 124501 (2009).
[10] [http://dcwww.camp.dtu.dk/campos/Dacapo/].
[11] [http://www.pwscf.org/].
[12] D. Vanderbilt, Phys. Rev. B **41**, 7892(R) (1990).
[13] J. H. Haeni, P. Irvin, W. Chang, R. Uecker, P. Reiche, Y. L. Li, S. Choudhury, W. Tian, M. E. Hawley, B. Craigo *et al.*, Nature (London) **430**, 758 (2004).
[14] H. Jonsson, G. Mills, and K. W. Jacobsen, in *Classical and Quantum Dynamics in Condensed Phase Simulations*, edited by B. J. Berne, G. Ciccotti, and D. F. Coker (World Scientific, Singapore, 1998), p. 385.
[15] C. J. Forst, C. R. Ashman, K. Schwarz, and P. E. Blochl, Nature (London) **427**, 53 (2003).
[16] A. A. Demkov, L. R. C. Fonseca, E. Verret, J. Tomfohr, and O. F. Sankey, Phys. Rev. B **71**, 195306 (2005).
[17] F. Niu and B. W. Wessels, J. Cryst. Growth **300**, 509 (2007).
[18] I. N. Yakovkin and M. Gutowski, Phys. Rev. B **70**, 165319 (2004).
[19] X. Zhang, A. A. Demkov, H. Li, X. Hu, Y. Wei, and J. Kulik, Phys. Rev. B **68**, 125323 (2003).
[20] L. F. Kourkoutis, C. S. Hellberg, V. Vaithyanathan, H. Li, M. K. Parker, K. E. Andersen, D. G. Schlom, and D. A. Muller, Phys. Rev. Lett. **100**, 036101 (2008).
[21] A. M. Kolpak, F. J. Walker, J. W. Reiner, Y. Segal, D. Su, M. S. Sawicki, C. C. Broadbridge, Z. Zhang, Y. Zhu, C. H. Ahn *et al.*, Phys. Rev. Lett. **105**, 217601 (2010).
[22] The energy of the isolated oxygen molecule is corrected to fix the well-known DFT overestimation of the O_2 binding energy, such that $E_{O_2} = 2E_O + \Delta H_f^{O_2}$, where E_O is the total energy of an isolated oxygen atom, and $\Delta H_f^{O_2}$ is the experimental value (Ref. 23) of the formation energy of O_2 from atomic oxygen at standard temperature and pressure.
[23] [http://webbook.nist.gov/].
[24] K. G. Godinho, J. J. Carey, B. J. Morgan, D. O. Scanlon, and G. W. Watson, J. Mater. Chem. **20**, 1086 (2010).
[25] K. Matsunaga, A. Nakamura, T. Yamamoto, and Y. Ikuhara, Phys. Rev. B **68**, 214102 (2003).
[26] N. Erdman, O. Warschkow, M. Asta, K. R. Poeppelmeier, D. E. Ellis, and L. D. Marks, J. Am. Chem. Soc. **125**, 10050 (2003).
[27] E. Takayama-Muromachi and A. Navrotsky, J. Solid State Chem. **72**, 244 (1988).
[28] A. M. Kolpak, D. Li, R. Shao, D. A. Bonnell, and A. M. Rappe, Phys. Rev. Lett. **101**, 036102 (2008).
[29] R. A. McKee, F. J. Walker, and M. F. Chisholm, Phys. Rev. Lett. **81**, 3014 (1998).
[30] X. D. Zhu, W. Si, X. X. Xi, and Q. Jiang, in *Recent Developments in Oxide & Metal Epitaxy Theory and Experiment*, MRS Symposia Proceedings No. 619 (Materials Research Society, Pittsburgh, 2000), p. 115.
[31] R. Merkle and J. Maier, Angew. Chem. **47**, 3874 (2008).
[32] R. Moos, W. Menesklou, and K. H. Hardtl, Appl. Phys. A **61**, 389 (1995).
[33] J. Claus, M. Leonhardt, and J. Maier, J. Phys. Chem. Solids **61**, 1199 (2000).
[34] P. Kruger and J. Pollmann, Phys. Rev. Lett. **74**, 1155 (1995).
[35] J. W. Reiner, A. Posadas, M. Wang, T. P. Ma, and C. H. Ahn, Microelectron. Eng. **85**, 36 (2007).
[36] I. Marozau, M. Dobeli, T. Lippert, F. Logvinovich, M. Mallepell, A. Shkabko, A. Weidenkaff, and A. Wokaun, Appl. Phys. A **89**, 933 (2007).
[37] J. Han, F. Wan, Z. Zhu, and W. Zhang, Appl. Phys. Lett. **90**, 031104 (2007).
[38] T. Schimizu, Solid State Commun. **102**, 523 (1997).
[39] A. M. Kolpak and S. Ismail-Beigi (unpublished).
[40] X. F. Wang, J. Wang, Q. Li, M. S. Moreno, X. Y. Zhou, J. Y. Dai, Y. Wang, and D. Tang, J. Phys. D **42**, 085409 (2009).
[41] S. B. Mi, C. L. Jia, V. Vaithyanathan, L. Houben, J. Schubert, D. G. Schlom, and K. Urban, Appl. Phys. Lett. **93**, 101913 (2008).